Journal of Materials Chemistry A

PAPER

View Article Online
View Journal | View Issue

Cite this: J. Mater. Chem. A, 2015, 3, 22627

Shell-thickness dependent electron transfer and relaxation in type-II core–shell CdS/TiO_2 structures with optimized photoelectrochemical performance

Sancan Han,[a] Ying-Chih Pu,[b] Lingxia Zheng,[a] Jin Zhong Zhang*[b] and Xiaosheng Fang*[a]

Received 7th September 2015
Accepted 28th September 2015

DOI: 10.1039/c5ta07100c

www.rsc.org/MaterialsA

Core–shell CdS/TiO_2 structures are promising for solar-to-fuel conversion applications because their ideal type-II band alignment helps effective charge transfer to form the CdS^+/TiO_2^- system. A better understanding of the charge carrier dynamics is critical to provide guiding principles for designing photoelectrochemical (PEC) devices. Hence, TiO_2 shell-thickness dependent charge carrier dynamics and competition between electron relaxation in CdS (*e.g.* recombination and trapping) and electron transfer from CdS to TiO_2 were investigated using ultrafast transient absorption (TA) spectroscopy. The results indicate that the CdS/TiO_2 nanocomposite with a molar ratio of 2 : 1 exhibits the highest electron transfer rate constant of $\bar{k}_{ET} = 2.71 \times 10^{10}$ s^{-1}, along with an electron relaxation rate of $\bar{k}_{CdS/TiO_2} = 3.43 \times 10^{10}$ s^{-1}, resulting in an electron transfer quantum efficiency of $Q_{ET} = 79\%$, which also corresponds to the best PEC hydrogen generation in the CdS/TiO_2 core–shell composites. However, the electron transfer rate decreases with increasing thickness of the TiO_2 shell consisting of aggregated nanoparticles. One possible explanation is that the CdS and TiO_2 form relatively larger, separate particles, or less conforming small particles, with poor interfaces with increasing TiO_2, thereby reducing electron transfer from CdS to TiO_2, which is supported by SEM, and TEM data and consistent with PEC results. The thickness and morphology dependence of electron transfer and relaxation provides new insight into the charge carrier dynamics in such composite structures, which is important for optimizing the efficiency of PEC for solar fuel generation applications.

1. Introduction

Nanocomposite materials have long been of strong interest due to their unique multifunctional properties that cannot be obtained in single-component structures.[1,2] In particular, core–shell nanocomposite structures have attracted considerable attention due to their potential applications in lithium storage,[3] solar cells,[4] photocatalysis,[5–7] electronics and bioimaging.[8,9] One type of core/shell structure of strong interest is that composed of two semiconductor materials with different bandgaps. One main advantage of such structures is that the shell provides a physical barrier between the optically active core and the surrounding medium, thus making the core less sensitive to environmental changes, surface effects, and photo-oxidation.[10,11] In addition, band alignment for effective charge transfer is of paramount importance in the design of photovoltaic and water splitting systems.[12,13] Type-II structures have appropriate band structures for forming a staggered alignment at the heterojunction, such that the band-edge energies of the conduction and valence bands (VBs) of the shell are either both higher or both lower than those of the core.[14,15] As a result, one carrier is mostly confined to the core, while the other is mostly confined to the shell, generating an energy gradient at the interface to spatially separate the electrons and holes.[11,16,17]

To date, type-II core–shell systems have been mainly based on large bandgap semiconductors, such as TiO_2, used as the core, coupled with CdS as the shell. It is rare to have a small bandgap semiconductor such as CdS as the core and a large bandgap semiconductor such as TiO_2 as the shell.[18–21] The latter type-II core–shell nanostructures, in which the lowest energy conduction band (CB) electron is mainly localized in the shell while the lowest energy valence-band hole is localized in the core, should not only enable fast electron transfer but also retard charge recombination because the shell can act as a tunneling barrier for the localized hole.[22] Hence, CdS core–TiO_2 shell nanocomposites, where photoexcitation results in an internal charge separation between the valence-band hole localized in the CdS core and the conduction-band electron in the TiO_2 shell to form the CdS^+/TiO_2^- system, should be more ideal for photocatalytic and PEC applications. Recently, there

[a]Department of Materials Science, Fudan University, Shanghai 200433, P. R. China. E-mail: xshfang@fudan.edu.cn

[b]Department of Chemistry and Biochemistry, University of California, Santa Cruz, California 95064, USA. E-mail: zhang@ucsc.edu

are a few reports about CdS core–TiO_2 shell structures, with the focus on the photocatalytic performance of one-dimensional (1D) CdS/TiO_2 systems, in which agglomeration of the samples results in unsatisfactory photocatalytic performance.[23–25] 1D nanostructures are mostly fabricated by chemical vapor deposition (CVD), which involves high temperature and long time, inhibiting large-scale application. Therefore, a facile and low-cost synthesis of CdS/TiO_2 core–shell nanocomposites is desired for practical applications. Furthermore, photoexcited carrier dynamics and charge separation properties of CdS core/TiO_2 shell nanocomposites are not well understood.

Herein, we synthesized uniform spherical CdS/TiO_2 core–shell nanoparticles with different TiO_2 shell thicknesses *via* a facile two-step solvothermal method. The PEC performance was investigated for pure CdS and CdS/TiO_2 composites with different molar ratios of CdS to TiO_2 (defined as 2 : 1 CdS/TiO_2, 1 : 1 CdS/TiO_2, and 1 : 2 CdS/TiO_2, respectively). Femtosecond transient absorption (TA) spectroscopy was used to investigate the electronic transfer and relaxation dynamics on ultrafast time scales as a function of the TiO_2 shell thickness. The competition between electron relaxation in CdS and electron transfer to TiO_2 plays a crucial role in the PEC performance. We report that the 2 : 1 CdS : TiO_2 sample exhibits the highest electron transfer rate and the best PEC performance, while the thicker TiO_2 shell seems to retard electron transfer and leads to lower PEC efficiency. This study provides insight into the mechanism of charge transfer in CdS/TiO_2 core/shell nanocomposite structures, which is important for designing new materials with improved PEC performance for energy conversion and other applications.

2. Experimental section

2.1 Materials

All chemicals were used as received without any further purification. $Cd(CH_3COO)_2 \cdot 2H_2O$ (Sinopharm Chemical Reagent Corp.), thiourea (Sinopharm Chemical Reagent Corp.), tetrabutyl titanate (Sinopharm Chemical Reagent Corp.), and analytical alcohol (98%, Sigma-Aldrich).

2.2 Synthesis of CdS/TiO_2 nanocomposites

Synthesis of CdS nanoparticles. The monodisperse CdS nanoparticles were first fabricated following a typical procedure:[26] $Cd(CH_3COO)_2$ (2.4 mmol, 0.6397 g) and thiourea (24 mmol, 1.82 g) were dissolved in 60 ml de-ionized water and stirred for 30 min to form a clear solution at room temperature. Then the mixture was transferred to a Teflon-lined autoclave (100 ml). Subsequently, it was heated to 200 °C for 5 h. After natural cooling, the precipitates were washed with de-ionized water and ethanol three times, respectively, and then dried in a vacuum oven at 60 °C for 6 h.

Synthesis of CdS/TiO_2 nanocomposites. The as-synthesized CdS nanoparticles (0.1 g) were dissolved in 40 ml absolute ethanol, followed by the addition of the desired volume of tetrabutyl titanate (TBOT). Then 24 ml deionized water was added dropwise with magnetic stirring. The mixture solution was kept stirring for another 2 h and was transferred to a Teflon-lined autoclave (100 ml). Afterwards, a hydrothermal reaction was conducted at 180 °C for 24 h in an electric oven. Finally, the samples were washed, and then dried in a vacuum oven at 60 °C for 6 h.

2.3 Characterization

The structure and morphology of the CdS and CdS/TiO_2 nanocomposites were characterized by field-emission scanning microscopy (FESEM, JSM-6701F), and transmission electron microscopy (TEM, JEM-2100F) was employed to analyze the thickness of the TiO_2 shell and composition of the samples. X-ray diffraction using Cu Kα radiation (XRD, Bruker D8-A25) and Raman spectroscopy (Raman spectra were recorded on a modified micro Raman Imaging Microscope (Renishaw, Inc), using a helium-neon laser operating at a wavelength of 632.8 nm.) were used to investigate the crystal and phase structure. The optical properties of the samples were characterized using a UV-visible spectrophotometer (Agilent Tech. Cary 60 UV-vis) and a photoluminescence spectrofluorometer (Perkin-Elmer model LS50B luminescence spectrometer). The excitation wavelength was chosen as 380 nm to excite the samples.

2.4 Photoelectrochemical test

The PEC measurements were carried out on a Sonartron 1280 B (Oakridge, TN), which were described before.[27] A 1000 W Xe lamp (Oriel Research Arc Lamp assembly # 69 924 and power supply # 69 920) was used as a white light source. All PEC measurements were carried out in a three electrode electrochemical cell, with a Ag/AgCl reference electrode and a Pt wire counter electrode. The samples were deposited on the FTO conductive glass by spin-coating at 2000 rpm for 40 s, and then annealed for 2 h at 350 °C to form the working electrodes. 0.25 M Na_2S and 0.35 Na_2SO_3 aqueous solution as the electrolyte was employed to maintain the stability of CdS and CdS/TiO_2 nanocomposites. Linear sweep voltammograms were measured at a scan rate of 5.0 mV s^{-1} at applied potential from −1.4 V to 0 V. IPCE was measured from 350 nm to 600 nm at an applied potential of −0.5 V (*vs.* Ag/AgCl), which was calculated according to the equation as follows:

$$\mathrm{IPCE} = \frac{1240J}{\lambda I_{\mathrm{light}}} \quad (1)$$

2.5 TA/TB pump-probe spectroscopy test

TA/TB pump-probe spectroscopy was conducted with a Quantronix laser system consisting of a Palitra-FS optical parametric amplifier pumped by an Integra-C Ti:Sapphire amplifier system, as described in detail previously.[28] Briefly, a pump wavelength of 400 nm, generated by using an optical parametric amplifier (OPA), was used to excite the samples with 73 nJ per pulse, which guarantees linear effects. And a white light continuum, which was stable from 430 nm to 800 nm with a pulse width of 100 fs, was used to probe the samples.

3. Results and discussion

3.1 Structure and morphological characterization

X-ray diffraction (XRD) was used to characterize the crystal structure and the crystallinity of the pure CdS and CdS/TiO_2 nanocomposites. Representative XRD patterns are shown in Fig. 1a. The pure CdS nanoparticles show a wurtzite structure (JCPDS card no. 75-1545) while the deposited TiO_2 can be assigned to the anatase structure (JCPDS no. 21-1272). However, the characteristic peaks of pure CdS are very similar to that of the CdS/TiO_2 nanocomposites due to the dominance of CdS contribution. The peaks of TiO_2 located at 25.25°, 37.94°, and 48.04°, indexed to (101), (004) and (200) planes, respectively, likely overlapped with the peaks of CdS at 24.87°, 36.92°, and 47.92°, which are indexed to (100), (102) and (103) planes, respectively, of pure CdS.

Hence, Raman spectroscopy was conducted to further confirm and identify the presence and crystallinity of TiO_2. As shown in Fig. 1b, the Raman peaks at 396.5 cm^{-1}, 513.1 cm^{-1} and 635.8 cm^{-1} can be assigned to B_{1g}, A_{1g} and E_g modes of anatase TiO_2, respectively, which is consistent with a previous study.[29] For CdS/TiO_2 nanocomposites, the peak intensities of B_{1g}, A_{1g} and E_g increase with the increasing amount of TiO_2, which is expected. Interestingly, the peak at 183.0 cm^{-1} (another E_g mode) exhibits a substantial red-shift phenomenon compared with that of standard anatase TiO_2 (146 cm^{-1},[29]). The formation of oxygen vacancies in TiO_2 crystals could lead to higher frequency of the anatase E_g mode (from 146 cm^{-1} to 183.0 cm^{-1}).[29,30] This high E_g frequency observed here could thus indicate a high density of oxygen vacancies of TiO_2 in CdS/TiO_2 nanocomposites. Oxygen vacancies acting as shallow donors in TiO_2 can improve the electrical conductivities and the donor densities, thus increasing the PEC performance.[31]

Fig. 2 shows the scanning electron microscopy (SEM) images of the pure CdS and CdS/TiO_2 nanocomposites, revealing that the CdS nanoparticles are spherical in shape and have a uniform morphology with a size of about 200 nm. As can be seen in Fig. 2b–d, the CdS nanoparticles are fully covered with TiO_2, forming a core–shell type nanocomposite. The diameter of the nanoparticles increased with TiO_2 coating, and the thickness of the TiO_2 shell increased with the increasing amount of tetrabutyl titanate (TBOT). However, overloading of TBOT in the synthesis led to the formation of irregular-shapes and aggregation of nanoparticles, resulting in the formation of relatively larger, separate TiO_2 particles with poor interfaces with CdS. The results suggest that the CdS/TiO_2 core–shell nanocomposites have been generated *via* a controlled two-step solvothermal process, and the thickness of the TiO_2 shell can be tuned by adjusting the volume of TBOT. The actual TiO_2 shell thickness was determined by high resolution transmission electron microscopy (TEM).

As shown in Fig. 3a, TEM results reveal relatively uniform pure CdS structures. Fig. 3b–d show CdS/TiO_2 structures with different shell thicknesses, average thicknesses of TiO_2 nanoparticle aggregated shells in 2 : 1 CdS/TiO_2, 1 : 1 CdS/TiO_2, and 1 : 2 CdS/TiO_2 nanocomposites are around 18 nm, 28 nm, and 50 nm, respectively. And the shell is composed of TiO_2 nanoparticles with an average size of ~7 nm in 2 : 1 CdS/TiO_2 core–shell nanocomposites, which are distributed relatively even over the surface of the CdS core. From the high magnification TEM

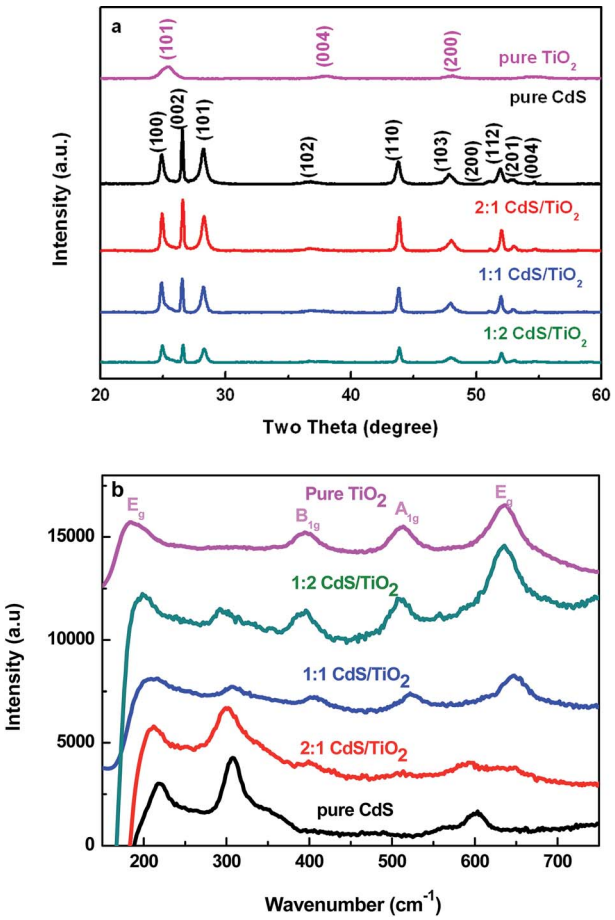

Fig. 1 (a) XRD and (b) Raman spectra of pure CdS and CdS/TiO_2 nanocomposites.

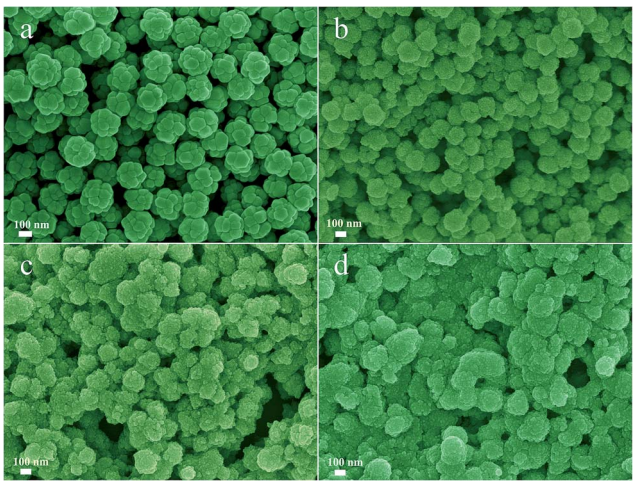

Fig. 2 SEM images of the pure CdS and CdS/TiO_2 nanocomposites. (a) CdS; (b) 2 : 1 CdS/TiO_2; (c) 1 : 1 CdS/TiO_2; (d) 1 : 2 CdS/TiO_2.

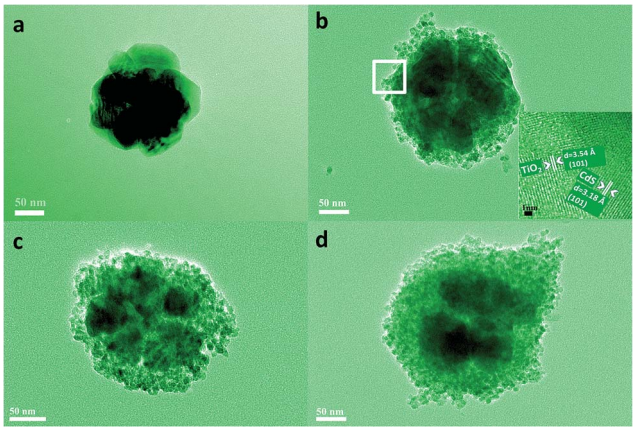

Fig. 3 Low-magnification TEM images of CdS/TiO_2 core–shell nanocomposites. (a) pure CdS; (b) 2 : 1 CdS/TiO_2; the inset corresponds to the lattice fringes of the white frame. (c) 1 : 1 CdS/TiO_2; (d) 1 : 2 CdS/TiO_2.

(HRTEM) image (the inset of Fig. 3b), the interplanar spacings of adjacent lattice fringes are estimated to be 0.318 nm and 0.354 nm and assigned to the (101) plane of CdS and (101) plane of TiO_2, respectively. In addition, free-standing TiO_2 nanoparticles were rarely observed, indicating the advantage of the current approach to obtaining CdS/TiO_2 core–shell nanocomposites. By this two step process, the TiO_2 shell consisting of aggregated nanoparticles grows preferentially on the CdS nanoparticle seeds rather than as separate nuclei in solution because the activation energy for heterogeneous nucleation is much lower than that for homogeneous nucleation.[24,26] On the other hand, TiO_2 nanoparticle aggregated shells represent a full coating on the CdS core in the CdS/TiO_2 nanocomposites, which indicates direct contact or good interfaces between CdS and TiO_2 that should result in strong coupling between them for achieving noticeable charge separation for PEC applications.[32] However, as the ratio of TiO_2 increased in the CdS/TiO_2 nanocomposites, *e.g.* the 1 : 2 CdS : TiO_2 ratio, the CdS and TiO_2 nanoparticles seem to be forming larger and separated particles, or less conforming, which will result in poor contact or interfaces between them and thereby affect electron transfer as well as PEC performance, as discussed later.

3.2 Optical characterization

The optical properties of the semiconductor nanocomposites may reflect their electronic transition behaviors,[33–35] therefore, we first collected the absorption and photoluminescence (PL) spectra of CdS and CdS/TiO_2 composites. As shown in Fig. 4a, the absorption peak for pure CdS centered at ~504 nm (2.46 eV) can be attributed to the electronic transition from the conduction band (CB) to the valence band (VB).[26] However, TiO_2 can only absorb the light in the ultraviolet (UV) region due to its larger bandgap (3.2 eV), the enhanced intensity of UV absorption in the CdS/TiO_2 core–shell nanostructures can be ascribed to the combination with TiO_2, which benefits the photoactivity compared with pure CdS. In Fig. 4b, the PL profile of pure CdS nanoparticles represented a broad feature with the peak

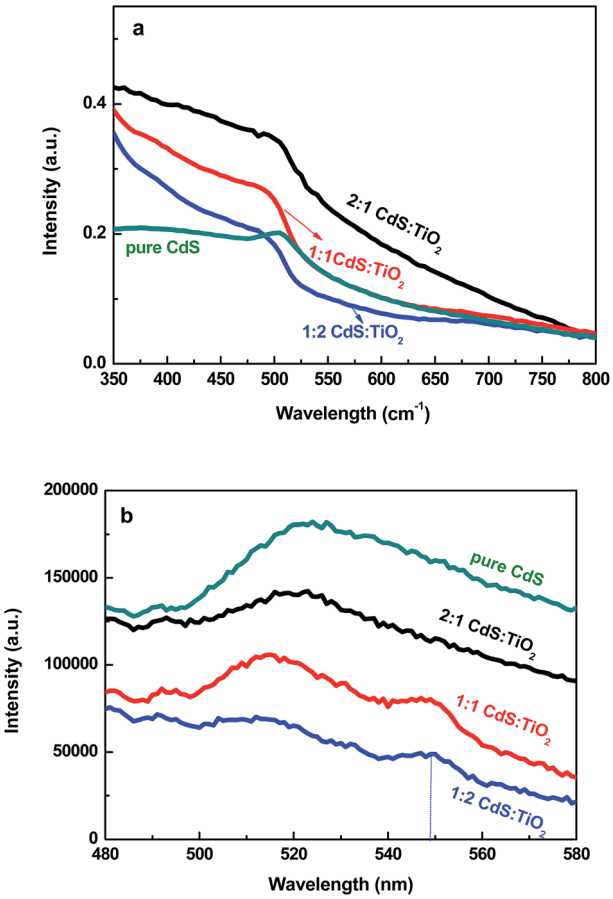

Fig. 4 (a) UV-vis absorption spectra and (b) photoluminescence (PL) spectra of pure CdS, 2 : 1 CdS/TiO_2, 1 : 1 CdS/TiO_2, and 1 : 2 CdS/TiO_2.

maximum at ~522 nm, which can be attributed to the electron–hole recombination from the CB to the VB. After the TiO_2 shell being coated on the CdS core, the PL profiles show similar emission features, but the PL intensities of the CdS/TiO_2 nanocomposites present a progressively decreased behavior as the TiO_2 shell thickness increased. The possible reason for reduction in the PL emission intensities of the CdS/TiO_2 nanocomposites may be due to the charge transfer from the CdS core to the TiO_2 shell due to the type-II band alignment, resulting in significant charge separation to reduce the radiative electron–hole recombination in the CdS core. However, the increase of the TiO_2 shell thickness could induce a red shift of the PL emission peak to ~550 nm, which may be due to the generation of trap states. Overall, modulation of the TiO_2 shell thickness can significantly change the optical properties of the CdS/TiO_2 nanocomposites, thereby altering the enhancement effect in photoactivity performance. So, the desired shell-thickness on core particles is vital for the preparation of high-quality nanoheterostructures.

3.3 PEC performance

The photoelectrochemical (PEC) performance of the pure CdS and CdS/TiO_2 core–shell nanocomposites as the photoanodes were studied in a three electrode electrochemical cell, which

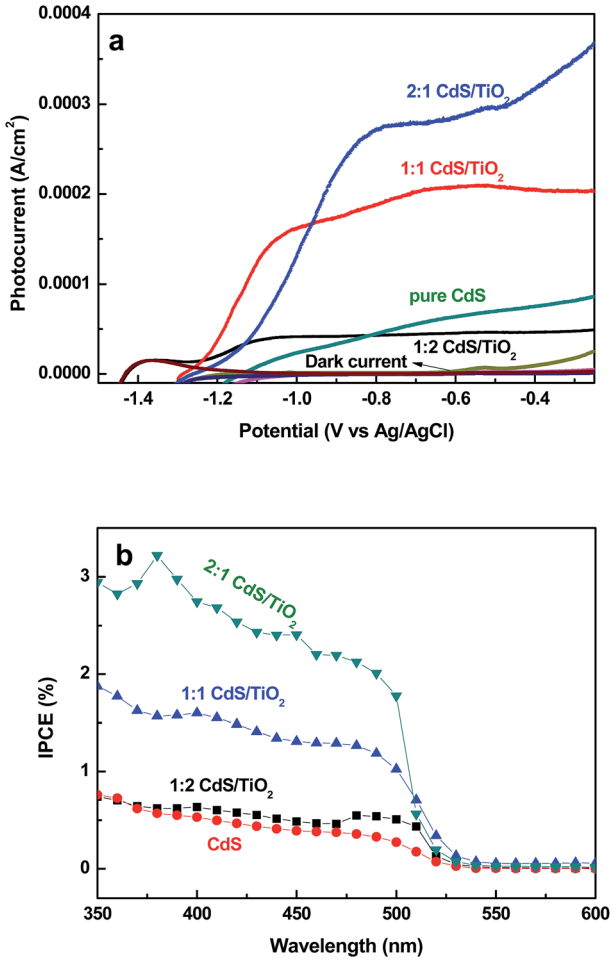

Fig. 5 Photoelectrochemical performance of CdS and CdS/TiO_2 core–shell nanocomposites with different shell thicknesses. (a) Photocurrent density *vs.* applied potential curve under the full-spectrum of simulated solar light. (b) Wavelength-dependent IPCE performance.

were performed by using a Ag/AgCl reference electrode and a Pt wire counter electrode. Fig. 5a shows a set of linear sweep voltammograms of CdS and CdS/TiO_2 electrodes recorded in 0.25 M Na_2S and 0.35 Na_2SO_3 electrolyte solution in the dark and under white light illumination (100 mW cm^{-2}). As shown in Fig. 5a, the onset potential was ~−1.2 V (*vs.* Ag/AgCl) and the maximum photocurrent density was ~0.1 mA cm^{-2} (at −0.25 V *vs.* Ag/AgCl) of the CdS nanoparticle photoanode. In contrast, the CdS/TiO_2 core–shell nanocomposites showed a significant enhancement in the photocurrent density under the same applied voltage. In addition, the negative shift of the onset potential to ~−1.3 and −1.45 V (*vs.* Ag/AgCl) of the CdS/TiO_2 core–shell nanocomposite electrodes was observed, which reveals that the TiO_2 shell coated on CdS could form the type-II energy band structure to further reduce the overpotential to perform PEC H_2 generation. The photocurrent densities of the CdS/TiO_2 core–shell nanocomposite electrodes of 2 : 1 CdS/TiO_2 and 1 : 1 CdS/TiO_2 were ~0.37 mA cm^{-2} and ~0.2 mA cm^{-2} (at −0.25 V *vs.* Ag/AgCl). However, the photocurrent density of the 1 : 2 CdS/TiO_2 electrode represented a dramatic decrease to ~0.05 mA cm^{-2}. Interestingly, the PEC performance of CdS/TiO_2 core–shell nanocomposite electrodes represents a progressively decreased behavior as the amount of TiO_2 is increased compared to CdS. This result confirmed that the positive role of the suitable TiO_2 shell coating on CdS nanoparticles can improve the PEC performance while too thick TiO_2 shell could decrease the efficiency of the CdS/TiO_2 core–shell nanocomposite electrode.

To further elucidate the role in improving the PEC performance of the CdS/TiO_2 electrodes, we collected incident photon-to-current conversion efficiency (IPCE) spectra of CdS and CdS/TiO_2 core–shell nanocomposites. As shown in Fig. 5b, the IPCE spectra of CdS and CdS/TiO_2 core–shell nanocomposites show similar profiles to their UV-vis absorption spectra. In addition, the 2 : 1 CdS/TiO_2 electrode showed the largest IPCE enhancement as compared to the CdS electrode. However, with the increase of the TiO_2 shell thickness, the IPCE in CdS/TiO_2 electrodes represented progressively decreased properties. The IPCE values at 450 nm, labeled as $IPCE_{450\ nm}$, were taken to compare the enhancement factor of the CdS and CdS/TiO_2 electrodes. The core–shell composite 2 : 1 CdS/TiO_2 electrode exhibited the highest photoconversion efficiency ($IPCE_{450\ nm}$ = 2.4%), exceeding that of pure CdS ($IPCE_{450\ nm}$ = 0.39%) by a factor of 6. The 1 : 1 CdS/TiO_2 composite showed an $IPCE_{450\ nm}$ = 1.30%, while the 1 : 2 CdS/TiO_2 sample has a lower value of 0.47%, which is almost the same value as that of the pure CdS electrode. The results show that introduction of an appropriate amount of TiO_2 onto the CdS core can achieve effective charge transfer from CdS to TiO_2, *i.e.*, in the formation of the CdS^+/TiO_2^- structure, resulting in overall better electron–hole separation to further enhance the photoconversion efficiency in comparison with pure CdS, however, the enhancement is strongly dependent on the thickness of the TiO_2 shell. More importantly, as the TiO_2 shell thickness increased, the IPCE spectra of CdS/TiO_2 electrodes showed a significant decrease in the UV region, which indicated that the charge collection and transportation in the TiO_2 shell are deteriorated as the thickness increased. There are two main factors to explain the phenomenon: (1) more grain boundaries in the TiO_2 nanoparticle aggregated shell, which could form the charge recombination center to reduce the photoconversion efficiency. (2) Formation of relatively larger, separate TiO_2 particles with poor interfaces, which reduce electron transfer from CdS to TiO_2. Therefore, a suitable TiO_2 shell coating on CdS could improve the charge separation to enhance the photoconversion efficiency as well as the PEC performance, while the overcoating of TiO_2 on CdS could generate relatively negative effects, resulting in a decreased efficiency of PEC H_2 generation.

3.4 Charge carrier dynamics by transient absorption spectroscopy

In order to better understand the mechanism behind the observed TiO_2 shell-thickness dependent PEC efficiencies, charge-carrier dynamics in the CdS/TiO_2 nanocomposite was studied using femtosecond transient absorption (TA) techniques. The TA spectra of CdS and CdS/TiO_2 samples were

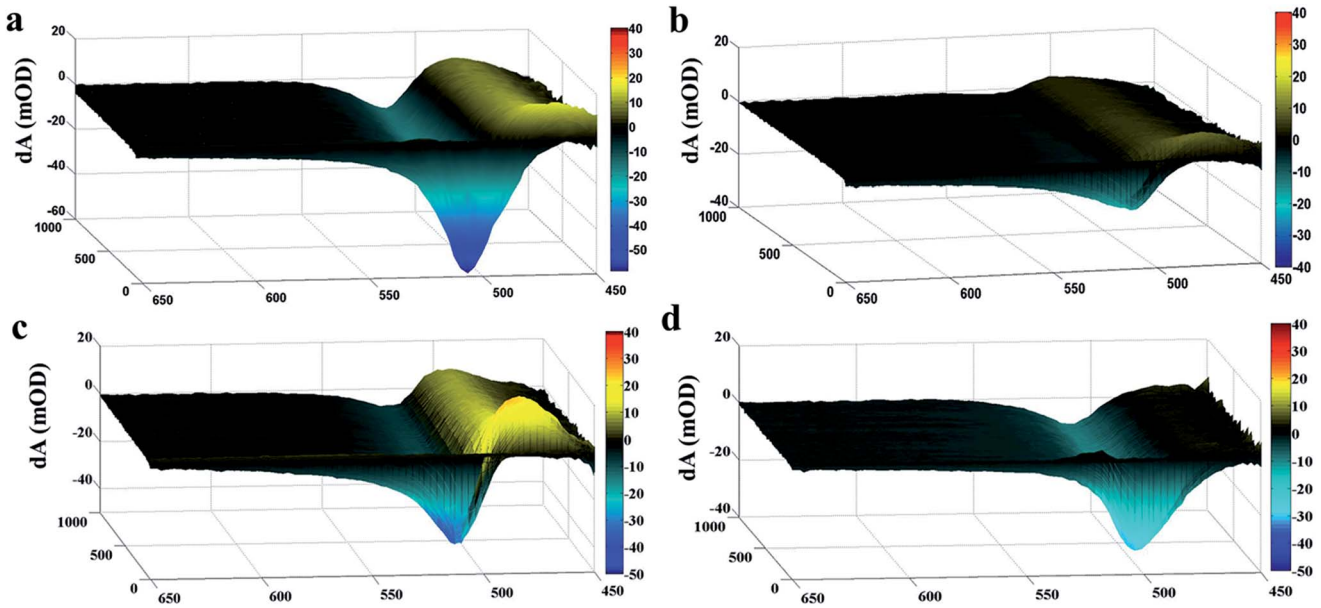

Fig. 6 Contour plots of transient absorption data after 400 nm excitation (73 nJ per pulse). (a) pure CdS; (b) 2 : 1 CdS/TiO_2 core–shell nanocomposites; (c) 1 : 1 CdS/TiO_2 core–shell nanocomposites; (d) 1 : 2 CdS/TiO_2 core–shell nanocomposites.

measured by using a 400 nm pump (73 nJ per pulse) and a white-light continuum probe (460–800 nm). Note that the chosen pump wavelength at 400 nm only excites the CdS. The wavelength dependent transient absorption (TA, excited state absorption) and transient bleach (TB, ground state depletion) profiles of CdS and CdS/TiO_2 samples are displayed as 3D plots in Fig. 6. The TA signals of the CdS and CdS/TiO_2 samples have similar profiles. The transient profiles at 460–500 nm showed a broad TA feature at short times, which can be attributed to the absorption of photoexcited electrons in the CB of CdS. A strong symmetric TB feature around 500–550 nm was also observed, which can be attributed to hole absorption in the VB of CdS. Over time, the recovery of the TB can be attributed to charge carrier (electron–hole) recombination or exciton decay.

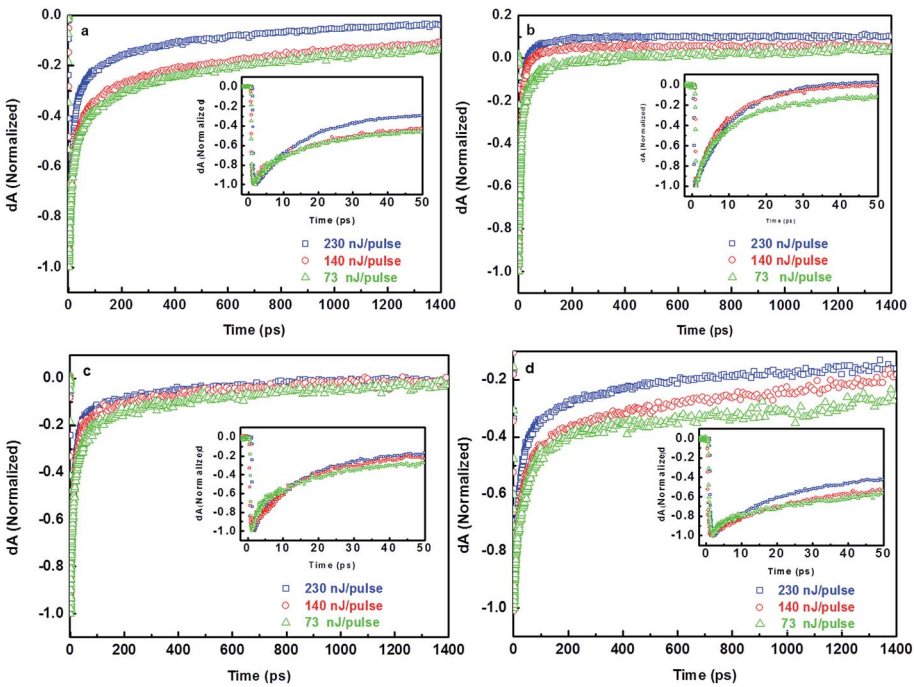

Fig. 7 TB decay profiles of (a) pure CdS nanoparticles; (b) 2 : 1 CdS/TiO_2 core–shell nanocomposites; (c) 1 : 1 CdS/TiO_2 core–shell nanocomposites; (d) 1 : 2 CdS/TiO_2 core–shell nanocomposites, with pump powers of 230 nJ per pulse, 140 nJ per pulse and 73 nJ per pulse. Insets: TB profiles from 0 to 50 ps.

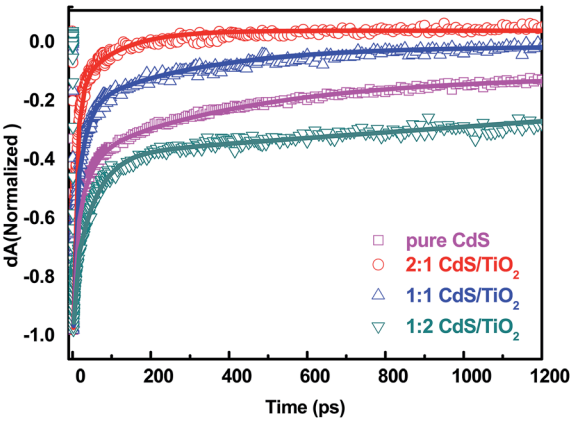

Fig. 8 Transient bleach kinetics of CdS and CdS/TiO_2 core–shell nanocomposites ($\lambda_{pump} = 400$ nm). The shorter photoexcited electron lifetime means better electron transfer from CdS to TiO_2.

Consequently, by tracking the TB recovery, we can characterize the recombination of photogenerated excitons or electron–hole pairs in CdS and CdS/TiO_2 samples. Before the detailed study of the exciton decay dynamics, we performed TA/TB measurements of the CdS and CdS/TiO_2 samples under three different pump powers of 230 nJ per pulse, 140 nJ per pulse, and 73 nJ per pulse to determine the possible power dependence of the dynamics since power dependent dynamics due to the nonlinear process can affect the interpretation of the results.[36–39] As shown in Fig. 7, the normalized maximum TB profiles of each sample represented a relatively significant difference as the pump power increased, however, the most similar recovery traces at a fast recovery component on a short time scale (0–20 ps) of all samples (insets of Fig. 7) were observed. The linear behavior on a short time scale indicates that the high-order kinetic processes at lower pump powers, such as exciton–exciton annihilation or Auger recombination, may not take place with a lifetime of hundreds of femtoseconds to a few picoseconds.[40–42] Hence, we focused on the comparison of the obtained TA data with the lowest pump power (73 nJ per pulse) to avoid the influence of high-order, nonlinear processes.

The TB feature of bandgap transition is proportional to the hole population.[37] Therefore, the single-wavelength recovery of the TB features can be assigned to the exciton recombination of the CdS and CdS/TiO_2 core–shell composites, and their relationship with the shell-thickness of TiO_2. The recoveries of the TB features of pure CdS and CdS/TiO_2 core–shell composites are shown in Fig. 8 (506 nm, 510 nm, 510 nm and 507 nm for pure CdS, 2 : 1 CdS/TiO_2, 1 : 1 CdS/TiO_2 and 1 : 2 CdS/TiO_2, respectively), and all the TB recoveries can be fit with a triple-exponential function. The lifetimes from the fitting are given in Table 1. For the pure CdS, the recovery of the fast component of 6 ± 0.4 ps can be attributed to relaxation or cooling of the free electrons and holes due to excess kinetic energy following generation. The medium (34 ± 2 ps) recovery component is attributed to non-radiative recombination through surface trap states.[43,44] The slow (450 ± 22 ps) recovery component can be attributed to the recombination of trapped electron–hole pairs.[45,46]

After the TiO_2 shell is coated on CdS, the TB recovery of the 2 : 1 CdS/TiO_2 composite can be fit with a triple exponential function with time constants of 2.4 ± 0.2 ps, 11 ± 0.6 ps, and 106 ± 6.6 ps. Similarly, the 1 : 1 CdS/TiO_2 nanocomposite has time constants of 3.0 ± 0.2 ps, 24 ± 1.5 ps, and 300 ± 23 ps, while the 1 : 2 CdS/TiO_2 sample has lifetimes of 4 ± 0.2 ps, 32 ± 0.4 ps and 485 ± 25 ps, respectively. The overall charge carrier decay for the 2 : 1 CdS/TiO_2 and 1 : 1 CdS/TiO_2 samples is faster compared to the pure CdS. However, the charge carrier decay of the 1 : 2 CdS/TiO_2 composites is almost the same as that of pure CdS. *i.e.*, the overall lifetime has the following order: 2 : 1 CdS/TiO_2 < 1 : 1 CdS/TiO_2 < pure CdS = 1 : 2 CdS/TiO_2. The competition between charge transfer (CT) and electron–hole recombination between the CdS core and TiO_2 shell plays a vital role in the overall decay or lifetime. For samples with a thin TiO_2 shell (18 nm, *i.e.*, 2 : 1 CdS/TiO_2), the decreased lifetime compared to pure CdS can be attributed to effective CT from CdS to TiO_2. When the shell gets thicker (28 nm, *i.e.*, 1 : 1 CdS/TiO_2), the charge transfer becomes less efficient due to the increased trap states with more TiO_2 on the surface of CdS and the formation of relatively separate large CdS and TiO_2 nanoparticles with poor interfaces, which results in the decreased lifetime compared with that of 2 : 1 CdS/TiO_2. For the thicker TiO_2 shell (50 nm, *i.e.*, 1 : 2 CdS/TiO_2), the CT seems to be insignificant. Because separate large CdS and TiO_2 nanoparticles with poor interfaces are dominant, which is more obvious for the 1 : 2 CdS/TiO_2 sample as shown in Fig. 3D, there is small probability for electron transfer from CdS to TiO_2.[32]

In order to gain further insight into the charge carrier dynamics of the CdS and CdS/TiO_2 core–shell composites, we performed more detailed analysis of fitting results by using an average lifetime. The average lifetime $\bar{\tau}$ is defined as follows:

Table 1 Fitting results of CdS and CdS/TiO_2 nanocomposites decay dynamics at low (73 nJ per pulse) pump power with percent intensity, lifetime (ps), and the calculated results of the average lifetime $\bar{\tau}$, the time-averaged decay rate constant $\bar{k}$ and time-averaged electron transfer rate constant $\bar{k}_{ET}$ according to eqn (1)–(4)

Samples	*A*1	τ_1 (ps)	*A*2	τ_2 (ps)	*A*3	τ_3 (ps)	$\bar{\tau}$ (ps)	$\bar{k}$ ($\times 10^9$ s^{-1})	$\bar{k}_{ET}$ ($\times 10^9$ s^{-1})
Pure CdS	0.35	6 ± 0.4	0.31	34 ± 2	0.28	450 ± 22	413	7.2	
2 : 1 CdS/TiO_2	0.37	2.4 ± 0.2	0.60	11.3 ± 0.6	0.20	106 ± 6.6	80	34.3	27.1
1 : 1 CdS/TiO_2	0.48	3 ± 0.2	0.45	24 ± 1.5	0.20	300 ± 23	253	13.2	6.0
1 : 2 CdS/TiO_2	0.13	4 ± 0.2	0.46	32 ± 0.4	0.21	485 ± 25	428	8.5	1.3

$$\bar{\tau} = \frac{\sum_{1}^{n} A_i \tau_i^2}{\sum_{1}^{n} A_i \tau_i} \quad (2)$$

Using the fitting results, the average lifetime $\bar{\tau}$ of the CdS and CdS/TiO_2 core–shell composites were calculated to be 413 ps, 80 ps, 253 ps and 428 ps for pure CdS, 2 : 1 CdS/TiO_2, 1 : 1 CdS/TiO_2 and 1 : 2 CdS/TiO_2, respectively. The time-averaged decay rate constant $\bar{k}$, and time-averaged electron transfer rate constant $\bar{k}_{ET}$ of the CdS and CdS/TiO_2 core–shell composites were defined as:[47]

$$\bar{k} = \frac{1}{\int_0^\infty \Delta A(t) \mathrm{d}t} \quad (3)$$

$$\bar{k}_{ET} = \bar{k}_{CdS/TiO_2} - \bar{k}_{CdS} \quad (4)$$

$$Q_{ET} = \frac{\bar{k}_{ET}}{\bar{k}_{CdS} + \bar{k}_{ET}} \quad (5)$$

$\bar{k}_{ET}$ and $\bar{k}_{CdS}$ are in the same order of magnitude, with both values at 10^9 s^{-1}. According to eqn (3) and (4), the 2 : 1 CdS/TiO_2 nanocomposite has the highest $\bar{k}_{ET}$ of 27.1 × 10^9 s^{-1} and Q_{ET} = 79.0%. The values of Q_{ET} of CdS/TiO_2 nanocomposites follow the order: 2 : 1 CdS/TiO_2 (79.0%) > 1 : 1 CdS/TiO_2 (45.0%) > 1 : 2 CdS/TiO_2 (15.3%), which illustrates that the efficiency of the electron transfer decreases with increasing thickness of the TiO_2 shell from ~18 nm to ~50 nm, which is consistent with the trend of lifetime. Because the CdS and TiO_2 form relatively larger, separate particles with poor interfaces with increasing TiO_2, resulting in the reduced $\bar{k}_{ET}$ and Q_{ET} of 1 : 1 CdS/TiO_2, which is exactly in agreement with the results of the performance of PEC.

Fig. 9 shows a schematic diagram to illustrate the relative energy level and the possible charge carrier relaxation pathway of the optimized CdS/TiO_2 core–shell nanocomposite (2 : 1 CdS/TiO_2). As an electron–hole pair is initially formed in CdS by absorbing a photon with energy greater than the bandgap. The exciton can then recombine through three possible pathways: first, some portion of the excitons undergoes nonradiative recombination through trap states (~10 ps lifetime). Second, some of the excitons undergo the interfacial charge transfer to achieve charge separation between CdS and TiO_2 with a $\bar{k}_{ET}$ of 27.1 × 10^9 s^{-1}. Third, the remaining excitons could recombine from the CB to VB at CdS with an ~100 ps lifetime by a non-radiative process. The optimized CdS/TiO_2 nanocomposite represents an ultrafast $\bar{k}_{ET}$, resulting in the effective electron collection of TiO_2, as well as the conductive electrode (FTO) to improve the PEC performance.

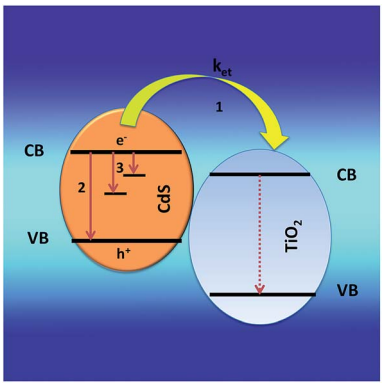

Fig. 9 Schematic diagram of the exciton relaxation process in CdS/TiO_2 core–shell composites.

4. Conclusion

We have successfully prepared CdS/TiO_2 core–shell composites with different TiO_2 shell thicknesses (~18 nm, ~28 nm, ~50 nm) using a facile two-step hydrothermal method. The PEC performance of the photoanodes which were made by the CdS/TiO_2 core–shell nanocomposites showed that the photoconversion efficiency followed the order: 2 : 1 CdS/TiO_2 > 1 : 1 CdS/TiO_2 > 1 : 2 CdS/TiO_2 = pure CdS. In addition, the exciton and charge carrier dynamics in the CdS/TiO_2 core–shell nanocomposites have been well investigated by using ultrafast TA spectroscopy. The obtained TA features by using the lowest pump power (73 nJ per pulse) were dominated by the exciton recombination that can be fit with a triple exponential recovery. Combined with the TA and mathematic fitting results, we observed that the 2 : 1 CdS/TiO_2 structure with the ~18 nm TiO_2 shell exhibits the highest charge carrier recombination rate because of an ultrafast $\bar{k}_{ET}$ of 27.1 × 10^9 s^{-1} and a high Q_{ET} of 79%. In addition, $\bar{k}_{ET}$ of the CdS/TiO_2 core–shell nanocomposites decreased with increasing thickness of the TiO_2 shell. This is tentatively attributed to the formation of relatively larger and more separate CdS and TiO_2 nanoparticles, or smaller nanoparticles of CdS and TiO_2 that are less conforming, with poorer interfaces or interfacial interaction. A good correlation between charge transfer dynamics and PEC performance of the present CdS/TiO_2 core–shell systems has been found, which is essential for further design of nanocomposites in different applications, including solar energy conversion or photodetectors.

Acknowledgements

The work was supported by the National Natural Science Foundation of China (Grant No. 51471051), Science and Technology Commission of Shanghai Municipality (13NM1400300), Shanghai Shu Guang Project (12SG01), and the Programs for Professor of Special Appointment (Eastern Scholar) at Shanghai Institutions of Higher Learning. Part of the experimental work has been carried out in Fudan Nanofabrication Laboratory. JZZ acknowledges the fund from the U.S. Department of Energy, UC-MEXUS/CONACYT and UCSC Faculty Special Research Fund.

References

1 A. O. Govorov, G. W. Bryant, W. Zhang, T. Skeini, J. Lee, N. A. Kotov, J. M. Slocik and R. R. Naik, *Nano Lett.*, 2006, **6**, 984.
2 J. S. Chen, L. A. Archer and X. W. Lou, *J. Mater. Chem.*, 2011, **21**, 9912.
3 J. S. Chen, D. Y. Luan, C. M. Li, F. Y. C. Boey, S. Z. Qiao and X. W. Lou, *Chem. Commun.*, 2010, **46**, 8252.
4 W. U. Huynh, J. J. Dittmer and A. P. Alivisatos, *Science*, 2002, **295**, 2425.
5 X. J. Xu, L. F. Hu, N. Gao, S. X. Liu, S. Wageh, A. A. Al-Ghamdi, A. Alshahrie and X. S. Fang, *Adv. Funct. Mater.*, 2015, **25**, 445.
6 Y. Wang, Y. N. Zhang, G. Zhao, H. Tian, H. Shi and T. Zhou, *ACS Appl. Mater. Interfaces*, 2012, **4**, 3965.
7 Z. Chen and Y. J. Xu, *ACS Appl. Mater. Interfaces*, 2013, **5**, 13353.
8 A. Patra, N. Venkatram, D. N. Rao and T. Radhakrishnan, *J. Phys. Chem. C*, 2008, **112**, 16269.
9 H. Lu, G. Yi, S. Zhao, D. Chen, L. H. Guo and J. Cheng, *J. Mater. Chem.*, 2004, **14**, 1336.
10 P. Reiss, M. Protiere and L. Li, *Small*, 2009, **5**, 154.
11 R. Ghosh Chaudhuri and S. Paria, *Chem. Rev.*, 2011, **112**, 2373.
12 K. F. Wu, W. E. Rodríguez-Córdoba, Z. Liu, H. Zhu and T. Lian, *ACS Nano*, 2013, **7**, 7173.
13 K. F. Wu, Q. Y. Li, Y. Y. Jia, J. R. McBride, Z. X. Xie and T. Lian, *ACS Nano*, 2015, **9**, 961.
14 S. S. Lo, T. Mirkovic, C. H. Chuang, C. Burda and G. D. Scholes, *Adv. Mater.*, 2011, **23**, 180.
15 H. McDaniel, M. Pelton, N. Oh and M. Shim, *J. Phys. Chem. Lett.*, 2012, **3**, 1094.
16 J. Bang, J. Park, J. H. Lee, N. Won, J. Nam, J. Lim, B. Y. Chang, H. J. Lee, B. Chon and J. Shin, *Chem. Mater.*, 2009, **22**, 233.
17 C. J. Dooley, S. D. Dimitrov and T. Fiebig, *J. Phys. Chem. C*, 2008, **112**, 12074.
18 K. Das and S. De, *J. Phys. Chem. C*, 2009, **113**, 3494.
19 J. Cao, J. Z. Sun, H. Y. Li, J. Hong and M. Wang, *J. Mater. Chem.*, 2004, **14**, 1203.
20 J. Luo, L. Ma, T. He, C. F. Ng, S. Wang, H. Sun and H. J. Fan, *J. Phys. Chem. C*, 2012, **116**, 11956.
21 J. Li, S. K. Cushing, P. Zheng, T. Senty, F. Meng, A. D. Bristow, A. Manivannan and N. Wu, *J. Am. Chem. Soc.*, 2014, **136**, 8438.
22 H. Zhu, N. Song and T. Lian, *J. Am. Chem.Soc.*, 2011, **133**, 8762.
23 L. Wu, Y. Zhang, X. J. Li and C. Cen, *Phys. Chem. Chem. Phys.*, 2014, **16**, 15339.
24 S. Liu, N. Zhang, Z. R. Tang and Y. J. Xu, *ACS Appl. Mater. Interfaces*, 2012, **4**, 6378.
25 N. Zhang, M. Q. Yang, S. Q. Liu, Y. G. Sun and Y. J. Xu, *Chem. Rev.*, 2015, **115**, 10307.
26 S. C. Han, L. F. Hu, N. Gao, A. A. Al-Ghamdi and X. S. Fang, *Adv. Funct. Mater.*, 2014, **24**, 3725.
27 A. Wolcott, W. A. Smith, T. R. Kuykendall, Y. Zhao and J. Z. Zhang, *Adv. Funct. Mater.*, 2009, **19**, 1849.
28 F. Wu, J. H. Yu, J. Joo, T. Hyeon and J. Z. Zhang, *Opt. Mater.*, 2007, **29**, 858.
29 L. Sang, Y. Zhao and C. Burda, *Chem. Rev.*, 2014, **114**, 9283.
30 J. Parker and R. Siegel, *Appl. Phys. Lett.*, 1990, **57**, 943.
31 G. Wang, Y. Ling and Y. Li, *Nanoscale*, 2012, **4**, 6682.
32 B. C. Fitzmorris, G. K. Larsen, D. A. Wheeler, Y. P. Zhao and J. Z. Zhang, *J. Phys. Chem. C*, 2012, **116**, 5033.
33 T. T. Yang, W. T. Chen, Y. J. Hsu, K. H. Wei, T. Y. Lin and T. W. Lin, *J. Phys. Chem. C*, 2010, **114**, 11414.
34 B. C. Fitzmorris, Y. C. Pu, J. K. Cooper, Y. F. Lin, Y. J. Hsu, Y. Li and J. Z. Zhang, *ACS Appl. Mater. Interfaces*, 2013, **5**, 2893.
35 V. Chakrapani, D. Baker and P. Kamat, *J. Am. Chem. Soc.*, 2011, **133**, 9607.
36 Y. C. Pu, M. G. Kibria, Z. Mi and J. Z. Zhang, *J. Phys. Chem. Lett.*, 2015, **6**, 2649.
37 J. K. Cooper, J. Cao and J. Z. Zhang, *ACS Appl. Mater. Interfaces*, 2013, **5**, 7544.
38 J. Z. Zhang, R. H. O'Neil and T. W. Roberti, *J. Phys. Chem.*, 1994, **98**, 3859.
39 T. W. Roberti, N. J. Cherepy and J. Z. Zhang, *J. Chem. Phys.*, 1998, **108**, 2143.
40 D. A. Wheeler and J. Z. Zhang, *Adv. Mater.*, 2013, **25**, 2878.
41 J. P. Zheng and H. S. Kwok, *Appl. Phys. Lett.*, 1994, **65**, 1151.
42 C. Burda, S. Link, M. B. Mohamed and M. El-Sayed, *J. Chem. Phys.*, 2002, **116**, 3828.
43 D. A. Wheeler, G. M. Wang, Y. C. Ling, Y. Li and J. Z. Zhang, *Energy Environ. Sci.*, 2012, **5**, 6682.
44 J. K. Cooper, Y. C. Ling, C. Longo, Y. Li and J. Z. Zhang, *J. Phys. Chem. C*, 2012, **116**, 17360.
45 Y. Ling, G. M. Wang, D. A. Wheeler, J. Z. Zhang and Y. Li, *Nano Lett.*, 2011, **11**, 2119.
46 V. A. Nadtochenko, N. N. Denisov, V. Y. Gak, F. E. Gostev, A. A. Titov, O. M. Sarkisov and V. V. Nikandrov, *Russ. Chem. Bull.*, 2002, **51**, 457.
47 M. B. Wilker, K. E. Shinopoulos, K. A. Brown, D. W. Mulder, P. W. King and G. Dukovic, *J. Am. Chem. Soc.*, 2014, **136**, 4316.